Lab on a Chip

This is an *Accepted Manuscript*, which has been through the Royal Society of Chemistry peer review process and has been accepted for publication.

Accepted Manuscripts are published online shortly after acceptance, before technical editing, formatting and proof reading. Using this free service, authors can make their results available to the community, in citable form, before we publish the edited article. We will replace this *Accepted Manuscript* with the edited and formatted *Advance Article* as soon as it is available.

You can find more information about *Accepted Manuscripts* in the **Information for Authors**.

A microtensiometer capable of measuring water potentials below -10 MPa

Vinay Pagay,[a] **Michael Santiago,**[b] **David A. Sessoms,**[c] **Erik J. Huber,**[b] **Olivier Vincent,**[c] **Amit Pharkya,**[c] **Thomas N. Corso,**[d] **Alan N. Lakso,**[e] **and Abraham D. Stroock**[*cf]

Abstract

Tensiometers sense the chemical potential of water (or water potential, Ψ_w) in an external phase of interest by measuring the pressure in an internal volume of liquid water in equilibrium with that phase. For sub-saturated phases, the internal pressure is below atmospheric and frequently negative; the liquid is under tension. Here, we present the initial characterization of a new tensiometer based on a microelectromechanical pressure sensor and a nanoporous membrane. We explain the mechanism of operation, fabrication, and calibration of this device. We show that these microtensiometers operate stably out to water potentials below -10 MPa, a tenfold extension of the range of current tensiometers. Finally, we present use of the device to perform an accurate measurement of the equation of state of liquid water at pressures down to -18 MPa. We conclude with a discussion of outstanding design considerations, and of the opportunities opened by the extended range of stability and the small form factor in sensing applications, and in fundamental studies of the thermodynamic properties of water.

[a] Department of Horticulture, Cornell University, Ithaca, NY 14853
 Present address: Department of Horticulture, Oregon State University, Central Point, OR 97502
[b] Sibley School of Mechanical and Aerospace Engineering, Cornell University, Ithaca, NY 14853
[c] School of Chemical and Biomolecular Engineering, Cornell University, Ithaca, NY 14853
[d] CorSolutions, LLC, Ithaca, NY 14850
[e] Department of Horticulture, NYSAES, Cornell University, Geneva, NY 14456
[f] Kavli Institute at Cornell for Nanoscale Science and Technology, Cornell University, Ithaca, NY 14853.
[*] Email: ads10@cornell.edu

Introduction

In both natural and technological contexts, the degree of saturation with respect to water often plays a central role in defining a system's properties and function. For example, in the atmosphere, relative humidity is a critical meteorological indicator, and is important to evaporative demand on soil, bodies of water, and the biosphere[1]. In the context of plants and agriculture, water saturation in the soil and atmosphere controls viability, growth potential, yield, and quality of crop.[2-4] In foods, water activity affects taste, texture, and stability with respect to bacterial and fungal growth.[5-8] In chemical and biological processes, the osmotic strength of aqueous solutions controls the kinetics and thermodynamics of reactions and the stability of cells, proteins, and materials.[5, 9-14] Additionally, the water status and dynamics of water in concrete is critical to final quality.[15]

The chemical potential of water, μ_w [J mol^{-1}], within a phase or host material provides the most generally useful measure of the degree of hydration. This thermodynamic state variable quantifies the free energy of water molecules and thus their accessibility for chemical reactions and physical exchange with other phases or materials. For example, regardless of the local mode of transport, we can express the driving force for mass transfer as a gradient of chemical potential. In the following, we will characterize the chemical potential of water with two convenient state variables: 1) activity, a_w, the relative humidity of a vapor in equilibrium with the phase of interest ($a_w = p/p_{sat}(T)$, where p and $p_{sat}(T)$ are the vapor pressure and saturation vapor pressure at temperature T, respectively); and, 2) Water potential, Ψ_w [MPa], the deviation of the chemical potential from its value at saturation divided by the molar volume of liquid water ($\Psi_w = (\mu_w - \mu_0(T))/v_{w,liq}$). Water potential is widely used in the plant and soil science communities. The typical water potential range of plants and soils is -0.001 > Ψ_w > -3.0 MPa (0.99999 > a_w > 0.978). In this paper, we describe a microelectromechanical system (MEMS) that promises to span this entire range

with a form factor that is compatible with *in situ* measurements within complex environments such as soils and plant tissues (Fig. 1).

For *in situ* measurements, many methods of hygrometry exist: capacitance,[16] resistance,[17] thermal conductivity,[18, 19] psychrometric,[20-22] and tensiometric.[23, 24] Capacitance, resistance, and dielectric methods measure the corresponding electronic property of a calibrated material within the sensor that is allowed to reach its equilibrium hydration with the phase of interest. These methods allow for small form factors (e.g. < 1 cm^2 sensing areas), but generally provide moderate to low accuracy (± ~0.02 in activity; ± ~3 MPa in water potential) for drier conditions (a_w < 0.9)[17, 25], and become less accurate above this range (e.g., ± 25% of measurement of water potential for the MPS-2 dielectric hygrometer by Decagon).[26] Despite their limited accuracy, resistive (gypsum block)[27] and capacitive (frequency domain reflectometry sensors)[28, 29] sensors are widely used for coarse measurements of water status in soils for irrigation scheduling.

Psychrometry, and thermocouple psychrometry in particular, has been the most heavily studied technique for *in situ* hygrometry in the environmental context.[30-33] Thermocouple psychrometry involves the measurement of the dew point temperature on a wetted thermocouple evaporating into a volume of air that separates it from the sample of interest; it is a transient, non-equilibrium process. The range of commercial psychrometers is reported by the manufacturer to be 0.999 to 0.93 in activity and -0.1 to -10 MPa in water potential with an accuracy of ± 0.001 in activity and ± 0.1 MPa in water potential.[34,35]

Tensiometers, as we will discuss in detail in the following section, operate on the principle of equilibration between a sample of interest and an internal volume of liquid water via a vapor gap and a microporous ceramic membrane (Fig. 1); capillarity within the pores of the membrane sustains a difference in pressure between the vapor and the internal liquid such that the water potential can be

measured as a difference in pressure across a diaphragm (Fig. 2b). Commercially-available tensiometers have a small range of 1 to 0.9988 in activity or 0 to -0.16 MPa in water potential with an excellent accuracy of $\pm$ 5×10^{-4} MPa in water potential;[36] they fail due to invasion of air or cavitation beyond this range. Despite the extremely limited range and large form factors of conventional tensiometers (sensing area > 10 cm^2), their unmatched accuracy near saturation means that they are used extensively to monitor the water potential in soils for irrigation scheduling for annual crops that require moist conditions to grow.[37] In research contexts, a number of groups have extended the range of operation of tensiometers. They have pursued two strategies: 1) Ridley and Burland first introduced the use of porous membranes with smaller pore sizes to achieve stability out to Ψ_w = -1.5 MPa ($a_w \cong$ 0.99);[38, 39] these "high capacitance tensiometers" have had similar form factors as those of conventional tensiometers; 2) Peck and Rabbidge first introduced the use of osmotic solutions within the internal volume of the tensiometers to extend the stability limit;[40, 41] more recently, this approach has been refined and demonstrated out to Ψ_w = -1.6 MPa (a_w = 0.988) with a reduced form factor (1.5 cm^2).[42-44]

The range, accuracy, and limitations of these various hygrometric approaches are summarized in Table 1.

TABLE 1

FIGURE 1

The tensiometric approach presents a promising route to accurate measurements of chemical potential across the range near saturation (a_w > 0.93, Ψ_w > -10 MPa), if the stability limit can be significantly extended. Furthermore, the development over the past decades of robust MEMS for sensing pressure[45] provides a route to reduce dramatically the form factor of tensiometers; a smaller sensor could allow for

measurements with higher spatial resolution and for embedding of the sensor within complex samples such as the vascular tissues of living plants. A MEMS approach could also help extend the stability limit by: 1) minimizing the internal volume of the liquid that is placed at reduced pressure; 2) minimizing the presence of impurities, which often lower the energetic barrier to nucleation; and, 3) allowing for the formation of the exchange membrane in well-defined, nanoporous materials such as porous silicon. In an effort to exploit these opportunities, we have developed a MEMS-based 'microtensiometer' (Fig. 1).

In this paper, we describe the operating principle and fabrication of a microtensiometer (Fig. 1), and characterize its stability, transient response, and use as a sensor in a laboratory environment. We conclude with a discussion of outstanding challenges and proposals of future applications that could address open questions in the thermodynamics of liquids, in plant and soil science (agriculture, plant physiology, ecology), and in materials such as food stuffs, and geotechnical materials such as concrete.

Background and theory

Working principle of tensiometry

FIGURE 2

Tensiometry is based on the coupling of liquid water to vapor via a wettable porous membrane. The concept is illustrated in Fig. 2. Chemical equilibration occurs between a macroscopic volume (large enough volume to surface area ratio to minimize wall interactions that could affect the thermodynamic properties of the liquid; smallest cavity dimension greater than ~ 1 μm)[46] of pure liquid inside a cavity within the tensiometer and a vapor that itself is in equilibrium with the chemical potential of the phase of interest outside the device (eqn (1); Fig. 2).

5

$$\mu_{w,liq}(T, P_{liq}) = \mu_{w,vap}(T, p_{vap}) = \mu_{sample} \tag{1}$$

When exposed to a sub-saturated external phase, the pure water in the tensiometer will evaporate from the external surface of the membrane. This loss of fluid will reduce the pressure in the bulk phase (P_{liq}) within the cavity (Figs. 2b-d). This reduction of pressure will lower the chemical potential (μ_{liq}) of the internal liquid. If the liquid phase remains intact, i.e., does not change phase to vapor (cavitate), the pressure will decrease until the internal and external chemical potentials are equal and transfer of water will cease. The pressure at which this equilibrium will occur can be found by expanding the expressions for the chemical potential of the pure liquid and vapor (ideal gas) in eqn (1):

$$\mu_0(T) + \int_{P_{atm}}^{P_{liq}} v_{w,liq}(P'_{liq}, T)dP'_{liq} = \mu_0(T) + RT\ln(a_{w,vap}) = \mu_{sample} \tag{2}$$

where $\mu_0(T)$ [J mol^{-1}] is the chemical potential of water on the vapor-liquid coexistence line (in the presence of P_{atm} of air) at temperature T [K], $v_{w,liq}$ [m^3 mol^{-1}] is the molar volume of the liquid, $R = 8.314$ [J mol^{-1} K^{-1}] is the ideal gas constant, and $a_{w,vap} = p_{vap}/p_{sat}(T)$ = relative humidity (%)/100 is the activity of the vapor at temperature, T. In eqn (2), we have assumed that the liquid is pure ($a_{w,liq} = 1$). If we further assume that the internal liquid is inextensible ($v_{w,liq}$ = constant), we can solve eqn (2) for the pressure of water inside the tensiometer cavity, P_{liq}, at equilibrium:

$$P_{liq} = P_{atm} + \frac{RT}{v_{w,liq}}\ln(a_{w,vap}) = P_{atm} + \frac{\mu_{sample} - \mu_0}{v_{w,liq}} = P_{atm} + \Psi_w \tag{3}$$

We can rearrange eqn (3) to provide relationships between the water potential of a phase of interest (Ψ_w), the pressure difference between the internal liquid and the atmosphere, and the activity of the vapor that mediates their equilibrium:[47]

$$\Psi_w = P_{liq} - P_{atm} = \frac{RT}{v_{w,liq}}\ln(a_{w,vap}) \tag{4}$$

6

The relations in eqn (4) hold within the approximation of constant molar volume of the liquid. We recognize in eqn (4) that the water potential is the pressure difference across the diaphragm of the tensiometer (Figs. 2a-b). In other words, a tensiometer provides a direct, approximate measurement of water potential. Eqn (4) also allows us to understand the unusual sensitivity of tensiometry near saturation: for $a_w = 1 + \Delta a_w$ with $\Delta a_w \ll 1$, we have at room temperature ($T = 293$ K):

$$\Psi_W \cong \frac{RT}{v_{w,liq}} \Delta a_w \cong 135 \Delta a_w \text{ [MPa]} \tag{5}$$

As an example, for a 1% reduction in activity from saturation ($\Delta a_w = -0.01$), the diaphragm of the tensiometer experiences a difference of pressure (from eqn (5)), $\Psi_w = P_{w,liq} - P_{atm} \cong -1.3$ MPa. With appropriate design of the diaphragm and strain gauge, pressure differences as small as 10^{-6} MPa can be achieved,[48] allowing for extreme sensitivity to small changes in saturation.

The approximation of constant molar volume that led to eqn (4) leads to an overestimate in the magnitude of the water potential, but this error is less than 0.5% for $\Psi_w > -22$ MPa ($a_w > 0.85$) at 20°C. As indicated in eqn (2), in order to achieve an exact determination of chemical potential, μ_{sample}, from the measurement of P_{liq} requires knowledge of the Equation of State (EoS) of the liquid along the isotherm at reduced pressure. The few existing measurements of thermodynamic properties of water at reduced pressure[49] suggest that the EoS of the International Association for the Properties of Water and Steam (IAPWS)[50, 51] provides accurate predictions at 20°C and down to $P_{liq} \cong -20$ MPa.

Stability limit of tensiometers

Eqn (3) states that the pressure in the bulk, internal liquid, P_{liq} will decrease as the activity or water potential in the external environment decreases. As this pressure drops below ambient, $P_{atm} \cong 0.1$ MPa, it becomes susceptible to the invasion of air through the pores and to cavitation (formation of gas bubbles). Invasion of air will occur through the membrane when:

$$P_{liq} - P_{atm} < \frac{2\sigma \cos\theta_r}{r_{p,max}} \tag{6}$$

where σ is the surface tension of water [0.072 N m^{-1}], θ_r [rad] is the receding contact angle of the liquid with the pore wall, $r_{p,max}$ [m] is the radius of the largest pore that spans the membrane. The threshold in eqn (6) represents the Young-Laplace pressure across a curved meniscus; for nanoscopic pores, it can only serve as a rough estimate of the threshold.[52] For $p_{sat} < P_{liq} < P_{atm}$, the internal liquid will be supersaturated with respect to air unless it has been degassed, and, therefore, be prone to cavitation by formation of bubbles of air. For lower pressures, $P_{liq} < p_{sat}$, the liquid will also be superheated and prone to cavitation via the formation of bubbles of vapor (boiling).[53] In the absence of pre-existing pockets of gas within the cavity, these two modes of cavitation will be kinetically limited and the liquid will be metastable.[53, 54] In conventional tensiometers, with macroscopic internal volumes and membranes with micrometer-scale pores, the stability limit tends to be $|P_{liq} - P_{atm}| < 0.1$ MPa, or $a_{w,vap} > 0.999$. Work by our group suggests that this limit can be extended significantly ($|P_{liq} - P_{atm}| > 20$ MPa; $a_{w,vap} < 0.86$) with the use of nanoporous membranes and smaller internal volumes.[55] This possibility motivated our construction of a microtensiometer to benefit from this extended range.

Piezoresistive pressure sensor

To measure the internal hydrostatic pressure of water, we adopted the widely-used diaphragm-based pressure transducer in which a pressure difference across the diaphragm results in its deflection (Fig. 2b), and the resulting strain is measured through piezoresistors. Specifically, our transducer consists of four doped polysilicon piezoresistors (Fig. 1b, R_1-R_4) in a Wheatstone bridge configuration (Fig. 1d) that sit atop a circular diaphragm (Figs. 1b-c). For resistances of nearly equal magnitude, the Wheatstone bridge response ($\Delta V_{out}/\Delta V_{in}$) as a function of applied difference in pressure (ΔP), diaphragm dimensions (r_d-

8

radius [m]; *h*-thickness [m]), and longitudinal and transverse piezoresistive coefficients, π_l and π_t [Pa^{-1}], can be calculated as:[56]

$$\frac{\Delta V_{out}}{\Delta V_{in}} = S\Delta P + \left(\frac{\Delta V_{out}}{\Delta V_{in}}\right)_{os} \tag{7}$$

$$S = \frac{3}{8}\frac{r_d^2}{h^2}(1-v)(\pi_l - \pi_t) \tag{8}$$

where S [Pa^{-1}] is the sensitivity, v is the Poisson Ratio of polysilicon (~ 0.23), $(\Delta V_{out}/\Delta V_{in})_{os}$ is the offset response at $\Delta P = 0$; the offset is due to small differences in the resistances of the branches of the Wheatstone bridge and of the contacts to the pads. Calibration of a pressure sensor involves measuring its values of S and $(\Delta V_{out}/\Delta V_{in})_{os}$ (Fig. 6). Eqn (8) assumes that the length of the piezoresistors is much less than the radius of the diaphragm. This assumption is reasonable for the two larger diaphragms (smaller relative size of piezoresistors), but starts to fail for the smaller diaphragms. See further discussion in sub-section *Pressure sensor calibration* under Results and Discussion.

Materials and Methods

Materials

Substrates: double-side polished silicon wafers (4" diameter, 325 μm thickness, *p*-type doping, resistivity range 1-10 Ω-cm and <111> orientation (University Wafer, http://www.universitywafer.com); Borofloat 33 glass wafer, double-side polished (4" diameter, 500 μm thickness, Prime grade; University Wafer, http:// www.universitywafer.com). Reagents: hydrofluoric acid (49% w/w, in H$_2$O; Sigma-Aldrich), ethanol (95% v/v; Sigma-Aldrich). Power supply for electrochemical etching: Hewlett Packard DC power supply (Model 6634B). Major microfabrication tools used in the cleanroom were: oxide and

thin-film deposition furnaces, photolithographic tools (resist spinner, contact aligner, wafer developer), wet etching reagents, dry etching tools (RF plasma etchers, oxygen plasma asher), PECVD thin film deposition, evaporator and sputtering tools (thin film metal deposition), high-temperature annealing tool, substrate bonder, and wafer dicing saw. Process characterization tools included profilometer, Filmmetrics thin film thickness analyzer, 4-point probe (wafer resistivity), and current-voltage (I-V) testing tool (resistor linearity).

Mask designs

Photolithographic masks for the fabrication of the microtensiometer were made in the cleanroom of the Cornell Nanoscale Science and Technology Facility (CNF), Ithaca, NY. Individual mask (images) were designed using L-Edit computer-aided design software (Tanner EDA, Monrovia, CA). Using a high-resolution pattern generator (Model DWL 2000, Heidelberg Instruments, Heidelberg, Germany), the mask images were transferred to a 5"×5" fused-silica (quartz) plate ("mask") coated with ~ 100 nm chromium and photoresist. Following pattern transfer (exposure), the photoresist on the exposed mask was developed and the chromium layer wet-etched. A complete list of masks used in the fabrication process is provided in the supplemental section S2.

Fabrication

FIGURE 3

Fabrication of the microtensiometer was done in the cleanroom of the CNF. The process flow for the fabrication of a microtensiometer is shown in Fig. 3; a detailed version can be found in supplemental section, Fig. S1. After standard RCA cleaning of the doped-silicon wafers, thermal oxide (SiO_2) was grown in a furnace at 1000°C to a thickness of ~ 1 μm for electrical isolation (Fig. 3-i). Doped $p+$ polysilicon (B_2H_6:SiH_4 ~0.045) was then deposited over the SiO_2 using a LPCVD furnace at 620°C and

10

400 mTorr to a thickness of ~ 900 nm for the piezoresistors. The wafer was then annealed in argon at 900°C for 30 min to enhance the polysilicon strain response and relax residual stresses. Typical resistivities of the LPCVD polysilicon were 18-23 Ω-cm (pre-annealing) and 9-14 Ω-cm (post-annealing). The polysilicon and SiO_2 layers were then patterned using photolithography and dry (plasma) etching to form the piezoresistors (dimensions 1100 μm $\times$ 30 μm $\times$ 1 μm) and metal insulation pattern, respectively (Fig. 3-ii). After removing the backside SiO_2 layer, a cavity was patterned and etched to a depth of ~25 μm on the backside of the silicon wafer using deep reactive ion etching (Bosch process; Fig. 3-iii). This process resulted in an effective diaphragm thickness of approximately, $h \cong 300$ μm.

The vapor exchange membrane of nanoporous silicon (PoSi) was then formed on the backside of the silicon wafer (Fig. 3-iv). We note that the use of wafers with <111> crystallographic orientation provided more reliable lateral connectivity of pores than the use of <100> orientation.[57] The setup for the fabrication of PoSi used a custom-built electrochemical etch cell made of polytetrafluoroethylene (PTFE or Teflon) (Fig. 4a). To ensure electrical contact of the silicon wafer to the anode, the wafers were dipped in 6:1 buffered oxide etch (BOE) solution for 1 min to remove the native oxide, and then coated with ~ 200 nm of aluminum by evaporation on the frontside of the wafer. The backside of the silicon wafer was then placed in contact with the etchant, a 50:50 (v/v) solution of 49% hydrofluoric acid (HF) and 95% ethanol (EtOH) in the etch cell.

FIGURE 4

Electrochemical etching was done under constant current density of 20 mA/cm^2 for 5 minutes using a Hewlett Packard DC power supply (Model 6634B), resulting in a PoSi layer of approximately 5 μm in thickness (Figs. 1c, 4b) with a pore diameter of 1-5 nm (Fig. 4d; as determined by porometry – data not shown). After removing the aluminum on the topside of the wafer, the PoSi was annealed at 700°C for 30

11

sec in an O_2 environment in order to replace the hydride-terminated silicon bonds (SiH_4) with O_2-terminated silicon to form SiO_2; this prevents the PoSi from degassing while bonding and filling with water.

After annealing, the PoSi side of the wafer was anodically-bonded to a 100 mm diameter and 500 µm thick borofloat glass wafer in vacuum at 400°C and 1200 V DC (Fig. 3-v) as follows: (i) the glass wafer was cleaned in a standard SC1 solution (29% NH_4OH and 30% H_2O_2 in water at 70°C) for 10 minutes to remove any organic materials, while the silicon wafer was cleaned by rinsing with acetone and isopropyl alcohol; (ii) the silicon and glass wafers were dried and plasma cleaned in an oxygen plasma asher (RF 150 W, 4 min, 70 sccm O_2); and, (iii) the silicon wafer (PoSi side) was anodically-bonded to the borofloat glass wafer using a substrate bonder (Model Sb8e, Süss Microtec, Garching, Germany).

After bonding, the electrical connections to the piezoresistors were formed. Following a short (~15 s) 30:1 BOE dip, a thin-film of aluminum (~250 nm) was evaporated on the frontside of the bonded wafer, patterned, and wet etched using a solution of phosphoric, acetic, and nitric acids @ 50°C to form the contact pads and wires (Figs. 1b-c, Fig. 3-vi). Aluminum was selected as the thin-film metal as it makes ohmic contact with polysilicon. Electrical isolation and protection of the electronics on the topside of the silicon wafer was achieved by depositing a stack of PECVD oxide (SiO_2; 400 nm), nitride (Si_3N_4; 200 nm), and oxynitride (SiO_2 + 15% Si_3N_4; 100 nm) at 200°C. This low deposition temperature was important to prevent debonding of the wafer. Vias were then opened over the metal pads using photolithography and dry etching (Fig. 3-vii). Lastly, individual devices (Figs. 1e-f) were released from the wafer by dicing with a wafer saw (Model 7100, Kulicke & Soffa, Singapore). A detailed process flow is given in the supplemental section, Fig. S1.

12

External electrical connections and measurements

A custom-built jig (dimensions: 2.5 cm × 2.5 cm × 1.3 cm; CorSolutions, Ithaca, NY) made of rigid acrylic with gold spring-loaded electrical pins (0.075" spring contact probe; Interconnect Devices, Inc.) was used for the sensor calibration (in positive pressures of air) and testing at both ambient and controlled relative humidities (see next section for calibration and testing setup; Fig. 5). The jig allowed for exchange of vapor through the nanoporous membrane while the pressure sensor was operated. The Wheatstone bridge of the pressure sensor was excited on pads C_1 and C_3, while the output voltage was measured on pads C_2 and C_4 (Fig. 1b). Pad C_3 was grounded, so that the voltage difference between C_1 and C_3 was always the positive applied voltage on P_1, V_{in}. An excitation voltage of 0.1 V was used for the pressure sensor, and based on an effective bridge resistance of 3 kΩ, resulted in a total current of less than 40 μA. Low operating currents were desirable to reduce Ohmic heating of the resistors. The jig (with the microtensiometer inside) was connected to an Agilent DC power supply (Model 6613C, Agilent Technologies, Palo Alto, CA) and an Agilent digital multimeter (DMM, Model 34401A). All voltages were recorded on the 100 mV setting of the multimeter. Both the DMM and power supply were connected to a digital acquisition (DAC) board (National Instruments, Austin, TX) and PC running LabView (v.7 Express, National Instruments Corp., Austin, TX).

Calibration of pressure sensor

FIGURE 5

Calibration of the electrical response to differences in pressure across the diaphragm (*S* in eqn (7)) was performed with the application of elevated, positive pressures of air to the outside of each device, with the cavity still filled with air. In order to block the flow of air into the device upon pressurization, the device was submerged in water for ~15 minutes such that the membrane took up water by capillarity, but the cavity remained filled with air. The liquid in the pores of the membrane blocked entry of air into the

internal cavity during exposure to elevated gas pressures (eqn (6)). This configuration leads to the same deflection of the diaphragm as occurs during operation of the tensiometer with liquid at reduced pressure within the cavity. For the calibration, a wired device was placed in a high-pressure chamber (leaf pressure chamber (PMS Instrument Co., Albany, OR) for pressures up to 3 MPa, or a HIP chamber (High Pressure Equipment Company, Erie, PA) for pressures up to 10 MPa) (Fig. 5a). To monitor pressure in the high pressure chamber, a precision pressure gauge (Model: TJE (5000 psig), Honeywell Sensotec, Columbus, OH) connected to a PC running LabView was used.

Filling

Following calibration, devices were placed in vacuum for at least four hours to dry the membrane and evacuate air from the internal cavity. This evacuation reduced the initial supersaturation with air of the liquid water that we forced into the cavity for device filling. We note that dissolution of a volume of air at atmospheric pressure into an equal volume of liquid water occurs at a pressure of ~ 6 MPa at room temperature (20°C/293.15°K); upon returning the solution to atmospheric pressure it would have a metastability equivalent to ~ 5.9 MPa of tension (calculated using data of air solubility in water at 293.15°K)[58]. The devices were filled by placing them in an HIP pressure chamber (same as used for calibration) filled entirely with deionized water (resistivity 7-18 MΩ) over 12-72 hours (Fig. 5b). The time to fill the devices depended on their internal volumes; the 3.4-mm diaphragm devices required over three days to fill completely at a pressure of 5 MPa. Higher filling pressures were avoided for these devices due to the risk of diaphragm fracture from the high applied strain. For the smaller diaphragm devices (0.7 and 1-mm radius), filling pressures over 10 MPa could be applied; these could be filled within 12 hours.

Operation

Testing of the sensor was done using the experimental setup depicted in Fig. 5c. The vapor activity of the chamber was controlled by delivering a stream of saturated vapor (generated by an evacuated reservoir of water at controlled temperature) into the environment chamber (Fig. 5c). The vapor activity to which the sensor was exposed was measured with a vacuum gauge (Model ASD 2002, Adixen, Annecy, France); this vapor pressure was varied by controlling the relative resistances to flow with valves upstream and downstream of the environment chamber (Fig. 5c). The environment chamber with the microtensiometer was placed in a temperature-controlled water bath to maintain isothermal conditions. With a defined temperature and vapor activity of the chamber, the liquid pressure inside the tensiometer was measured; this pressure was equivalent to the water potential (Ψ_w) or chemical potential (μ_w) at the given temperature: $\mu_w(a_w, T) \leftrightarrow P(a_w, T)$. Estimates of measurement uncertainty (error) of Ψ_w and a_w were obtained by statistical analysis of the uncertainties associated with individual sources of measurement error, i.e. from instrument accuracy. Pearson's chi-squared (χ^2) "goodness of fit" analysis was done to compare the experimental values of Ψ_w with IAPWS-95 values at 20°C.[50]

Results and discussion

Pressure sensor calibration

Fig. 6a shows the adjusted voltage response shifted by the observed offsets (($\Delta V_{out}/\Delta V_{in}$)-($\Delta V_{out}/\Delta V_{in}$)$_{os}$ – see eqn (7)) of four microtensiometers with diaphragms of different radii to the application of elevated gas pressure (see *Calibration* in Methods); all four devices were from the same wafer. All pressure sensors showed excellent linearity up to the highest pressures tested. Devices with

larger diaphragms had a lower pressure limit for fracture compared to devices with smaller diaphragms and hence were calibrated to lower pressures. As predicted by eqn (8), increasing the radius of the diaphragm increased the sensitivity.

FIGURE 6

TABLE 2

Fig. 6b presents the sensitivity, S (slopes from Fig. 6a) as a function of the square of the diaphragm radius; the values of S are listed in Table 2. The linearity of this plot indicates that the electromechanical response was consistent across these four devices taken from different locations on the wafer. Based on eqn (8), we find a piezoresistive coefficient $(1 - \nu)(\pi_l - \pi_t)$ of 1.7×10^{-10} Pa^{-1}. This value is consistent with values reported in the literature for p-type polysilicon (1.3×10^{-10} Pa^{-1} to 1.8×10^{-10} Pa^{-1}). [59, 60] We note that the responses of the smallest two diaphragms (0.7 and 1 mm-radius) fall below the best fit line. We expect the weaker response of these smaller devices was due to the large ratio of the length of the piezoresistors to the radius of the diaphragm; the average strain experienced by the piezoresistive elements decreases as this ratio increases.[61]

In Table 2, we provide estimates of the uncertainty in pressure for the different sizes of diaphragm. In our analysis of uncertainty from both the calibration and measurement processes, we found that the largest contributions came from the propagation of uncertainties of our voltage source (0.06 mV V^{-1}) and voltmeter (0.04 μV V^{-1}) (based on manufacturers' specifications); together these give an uncertainty of 0.07 mV V^{-1}. When transformed into pressures with the diaphragm-specific sensitivities, the values range from 0.78 MPa for the smallest diaphragm to 0.010 MPa for the largest diaphragm (Table 2, fourth column). For all diaphragm sizes, the uncertainty is ~1% of the full scale. We note that, even for the largest diaphragm with the highest sensitivity, the magnitude of the uncertainty is too large to resolve the

16

smallest, relevant deviations from saturation that are observed in soils ($\Psi_w \sim -10^{-3}$). The uncertainties of

the microtensiometer could be decreased significantly with more appropriate choices of electronic

instruments and more careful balancing of the Wheatstone bridge (i.e., to allow for the selection of a

smaller voltage scale on the voltmeter). State of art methods in bridge measurements suggest that we

should be able to reduce the uncertainty toward 0.01 % of full scale.[62] Appropriate implementation should

allow a single diaphragm size to cover most of the range required for environmental contexts (-10 MPa <

Ψ_w < -0.001).

FIGURE 7

Fig. 7 presents three calibration curves (as in Fig. 6) of the same device at three different

temperatures: 0.5°C, 10°C, and 20°C. The response was highly linear ($R^2 > 0.999$) at each temperature.

The lack of an obvious trend in the offset, $(\Delta V_{out}/\Delta V_{in})_{os}$, or sensitivity, S, with temperature indicates that

the balance of the bridge was adequate to limit the impact of the temperature-dependence of polysilicon

piezoresistors (0.01% °C^{-1} or 0.1 mV V^{-1} °C^{-1} in the offset for a single resistor).[63] In our experience,

unbalanced bridges (e.g., due to fabrication errors, poor contact at pads, or damaged resistors) led to much

stronger temperature-dependence. The change in sensitivity across these runs, $\delta S \sim 1.4 \times 10^{-2}$ mV V^{-1} MPa^{-1}, implies an uncertainty of 1.4% of the calibrated response. This uncertainty is compatible with that

predicted based on the specifications of our instruments (Table 2) and should be reduced with improved

implementation of our bridge measurements.

Membrane stability limit

FIGURE 8

Following calibration and filling with degassed water, the stability limits of microtensiometers were tested by exposing water-filled devices to ambient air (T ~ 20°C, a_w ~ 0.6 ≡ P_{liq} ≅ -54 MPa; eqn (6)). Fig. 8a shows the time-dependent response of a microtensiometer with a 1-mm radius diaphragm during drying; the voltage response ($\Delta V_{out}/\Delta V_{in}$) is shown on the left axis and the calibrated pressure on the right axis. After a period of ~ 35 minutes, the device cavitated and the response returned rapidly toward its baseline. In this extreme case, cavitation occurred at a liquid pressure approaching -33 MPa. To the best of our knowledge, this represents the largest tension ever recorded directly (as a mechanical stress) within a liquid by any method.[64] Fig. 8b presents a histogram of the stability limits measured for 15 independent experiments with 10 different devices. No device failed at a pressure above -10 MPa and most held to beyond -15 MPa. We note that we stored filled devices in containers with sub-saturated vapor ($a_{w,vap}$ = 0.95; Ψ_w = -6.9 MPa) for periods of several months without observing cavitation. From this observation and others,[54,64, 65] we expect the microtensiometers to be stable for extended periods when exposed to water potentials above their threshold (i.e., Ψ_w > -10 MPa). This range of stability is an order of magnitude larger than that reported previously for tensiometers.[36]

Most devices we tested were able to withstand multiple cycles (> 5) of filling and cavitation. On occasion, particularly for devices with large diaphragms (2 and 3.4 mm-radii), cavitation led to de-bonding at the interface between glass and silicon. The perturbation due to cavitation sometimes shifted the zero of the Wheatstone bridge, as can be seen in the time-traces in Fig. 8a. Such shifts may have occurred due to changes in the contact resistances leading to the piezoresistors during the rapid release of tension.

One can gain an appreciation for the violence of the cavitation process in the snapshot from a high speed video presented in Fig. 8c (see supplemental movie). This frame is from ~ 0.3 ms after the onset of

cavitation of a microtensiometer with a 3.4 mm-radius diaphragm as viewed through the glass (rear) side. The lighter grey regions are clouds of gas bubbles that were advected through the cavity.

We cannot draw any definitive conclusions about the mechanism of cavitation in these devices, but our experience with these membranes suggests that it occurred by heterogeneous nucleation.[53] In a related study involving porous silicon membranes formed by the same method,[65] we observed cavitation in this same range of tensions when the system was submerged in osmotic solutions; this observation tends to exclude invasion of air through the porous membrane as the origin of cavitation. We also note that the predicted pressure for the invasion of air through the pores is -58 MPa (via eqn (6) with $2r_p < 5$ nm and a receding contact angle, $\theta_r = 0°$) and is thus compatible with the hypothesis that cavitation occurred by a distinct mechanism in the observed range of stability limits. Previous measurements of the stability of water by our group by vapor-liquid equilibrium through organic membranes[54] and by others using a variety of methods[66] have also found a limit between -20 and -30 MPa. These considerations suggest that we could increase the diameter of the pores in the membrane without compromising the stability limit.

Transient responses to sub-saturated vapor

FIGURE 9

In order to characterize the transient response of the microtensiometer to external changes in activity, calibrated microtensiometers of all sizes (from the same wafer) were filled with water and exposed to a step change in vapor pressure in the vacuum chamber (Fig. 5c). The time constant, τ, associated with the transient response was calculated from the slope of the natural log plot of the unaccomplished change in the difference in pressure across the diaphragm (Fig. 9). We believe that these responses are intrinsic to the devices and not controlled by the external rates of mass transfer. We base this conclusion on rapid high rates of evaporation into a vacuum (Fig. 5c) and the fact that we observed the same rates when

19

devices under tension were allowed to relax in pure liquid water. The time constants for equilibration grew with the radius of the diaphragm and hence volume of liquid water inside the internal cavity. The transients of the 2 and 3.4 mm-radius devices were many hours long; such slow response means that these more sensitive devices would be impractical for many applications in environmental sensing in which characteristic changes of water potential occur due to, for example, diurnal changes in evaporative demand. The smaller diaphragms provide more reasonable relaxation times (one to a few hours) for some environmental sensing applications, but would still be too slow to capture all relevant time-scales. We expect that we will be able to reduce these time constants by lowering the resistance of the membrane (e.g., by decreasing the distance from the cavity to the edge and increasing the pore size) and minimizing the internal volume of water. We will provide a more complete analysis of the transport processes in the microtensiometer in a future paper.

Response to sub-saturated salts and vapors

FIGURE 10

The response of a microtensiometer with a 1-mm radius diaphragm to sub-saturated vapors was tested using an environment chamber with controlled vapor pressures in vacuum (Fig. 5c). We monitored the temperature, total vacuum pressure, and tensiometer response as we lowered the vapor pressure from saturation in steps such that the tensiometer equilibrated at each plateau. In this manner, we measured the equation of state in the form $P_{liq}(a_{w,vap}, T)$ along an isotherm into negative pressure. The microtensiometer response (Fig. 10, filled squares) agrees well ($R^2 > 0.998$) with predictions based on the internationally accepted equation of state (EoS) of water (IAPWS-95).[50] The large uncertainties in the activity arise due to the propagation of the uncertainty in temperature through eqn (4). In the only previous experimental measurement of the EoS to pressures below -10 MPa, Davitt et al. also found good agreement with

IAPWS-95 along the 20°C isotherm with an acoustic technique.[49] The data in Fig. 10 demonstrate the

potential of microtensiometers to provide accurate measurements of water potential to values well beyond

-10 MPa (a_w = 0.93). This range spans the relevant values in plants and soils[2-4] and covers an important

regime for other contexts such as geotechnical engineering,[67] meteorology[1], and food science,[6] and opens

a path to quantitative studies of the properties of metastable liquid water.[66] We note that χ^2 = 0.13 for the

measured pressures and the IAPWS-95 EoS; this low value suggests that we have over-estimated the

magnitude of the uncertainties.

Conclusions

In summary, we have presented the fabrication, operation, and characterization of a first generation

microtensiometer. Our MEMS design dramatically reduced the form factor of the device relative to

conventional tensiometers. The reduced dimensions will allow for unprecedented applications of

tensiometry for *in situ* measurements of water potential in living systems and for increased spatial

resolution. Our use of a nano-porous membrane extended the range of function by more than an order of

magnitude relative to current technologies. This range spans the relevant values in plants and soils[2-4] and

covers an important regime for other contexts such as geotechnical engineering,[67] meteorology[1], and food

science.[6] It further opens a path to quantitative studies of the properties of metastable liquid water under

tension.[66]

In our work with this first generation microtensiometer, we have identified a number of

modifications that will improve the performance: 1) to reduce transient response times, we should lower

the hydraulic resistance of the nanoporous membrane and the volumes of liquid within the internal cavity

and membrane; 2) to correct the water potential measurement in non-isothermal environments, we should

measure gradients in temperature between the source and the device using an integrated thermometer; 3) to improve the signal to noise ratio, we should minimize the offset response by fully balancing the Wheatstone bridge, and employ a more stable voltage source and voltmeter; and 4) to protect the membrane and the electronics from chemical and mechanical damage, we should develop application-specific packaging strategies. We are currently pursuing these modifications in order to realize the full potential of the microtensiometer as a tool for measurement of water potential in physical, biological, and environmental applications.

Acknowledgements

References

1.   J. Peixoto and A. H. Oort, *Journal of Climate*, 1996, **9**, 3443-3463.

2.   H. G. Jones, *Plants and microclimate : a quantitative approach to environmental plant physiology*, Cambridge University Press, Cambridge England ; New York, NY, USA, 1992.

3.   P. A. Shirke and U. V. Pathre, *Journal of Experimental Botany*, 2004, **55**, 2111-2120.

4.   T. Hirasawa and T. C. Hsiao, *Field Crops Research*, 1999, **62**, 53-62.

5.   M. J. Blandamer, J. B. F. N. Engberts, P. T. Gleeson and J. C. R. Reis, *Chem Soc Rev*, 2005, **34**, 440-458.

6.   J. A. Troller and J. H. B. Christian, *Water activity and food*, Academic Press, New York, 1978.

7.   N. Abdullah, A. Nawawi and I. Othman, *Journal of Stored Products Research*, 2000, **36**, 47-54.

8.   G. Ayerst, *Journal of Stored Products Research*, 1969, **5**, 127-141.

9.   A. Schiraldi, D. Fessas and M. Signorelli, *Polish Journal of Food and Nutrition Sciences*, 2012, **62**, 5-13.

10.   E. Wehtje and P. Adlercreutz, *Biotechnology and Bioengineering*, 1997, **55**, 798-806.

11.   V. Gekas, C. Gonzalez, A. Sereno, A. Chiralt and P. Fito, *International Journal of Food Properties*, 1998, **1**, 95-112.

12.   N. Asaad, M. J. den Otter and J. B. F. N. Engberts, *Org Biomol Chem*, 2004, **2**, 1404-1412.

13.   N. Asaad and J. B. F. N. Engberts, *J Am Chem Soc*, 2003, **125**, 6874-6875.

14.   M. Starzak and M. Mathlouthi, *Food Chemistry*, 2006, **96**, 346-370.

15.   K. C. Hover, *Constr Build Mater*, 2011, **25**, 3003-3013.

16.   L. Makkonen and T. Laakso, *Boundary-Layer Meteorology*, 2005, **116**, 131-147.

17.   F. Aziz, M. H. Sayyad, K. Sulaiman, B. H. Majlis, K. S. Karimov, Z. Ahmad and G. Sugandi, *Measurement Science & Technology*, 2012, **23**.

18.   M. W. Vandegehuchte and K. Steppe, *Functional Plant Biology*, 2013, **40**, 213-223.

19.   D. Roveti, *Sensors Magazine*, July 2001.

20.   G. J. W. Visscher, *Measurement Science & Technology*, 1995, **6**, 1451-1461.

21.   S. D. Wullschleger, M. A. Dixon and D. M. Oosterhuis, *Plant Cell and Environment*, 1988, **11**, 199-203.

22.   C. G. Enfield and J. J. C. Hsieh, *Water Resources Research*, 1971, **7**, 1349-1353.

23.   L. A. Richards, *Soil Science*, 1942, **53**, 241-248.

24.   F. J. Veihmeyer, N. E. Edlefsen and A. H. Hendrickson, *Plant Physiology*, 1943, **18**, 66-78.

25.   C. L. Cutting, A. C. Jason and J. L. Wood, *Journal of Scientific Instruments*, 1955, **32**, 425-431.

26.   Decagon Devices, AquaLab dew point water activity meter 4TE, MPS-2 dielectric water potential sensor, http://www.aqualab.com; http://www.decagon.com, Accessed December 3, 2013.

27.   E. Stenitzer, *Theoretical and Applied Climatology*, 1993, **48**, 159-165.

28.   A. Fares and A. K. Alva, *Soil Sci Soc Am J*, 2000, **64**, 311-318.

29.   L. R. Parsons and W. M. Bandaranayake, *Soil Sci. Soc. Am. J.*, 2009, **73**, 1378-1385.

30.   D. Spanner, *Journal of Experimental Botany*, 1951, **2**, 145-168.

31.   L. Richards and G. Ogata, *Science*, 1958, **128**, 1089-1090.

32.   Psychrometry in Water Relations Research, Utah Agricultural Experimental Station, 1972.

33.   M. Dixon and M. Tyree, *Plant, Cell & Environment*, 1984, **7**, 693-697.

34.   ICT International, PSY1 Psychrometer, http://www.ictinternational.com.au.

35.   M. A. Dixon and M. T. Tyree, *Plant Cell and Environment*, 1984, **7**, 693-697.

36.   Delta-T Devices, SWT-4 and SWT-5 - Water Filled Tensiometers, http://www.delta-t.co.uk, Accessed December 3, 2013.

37.   S. J. Richards and A. W. Marsh, *Proc. Soil Sci. Soc. Amer.*, 1961, **25**, 65-69.

38.   A. M. Ridley, J. B. Burland, F. A. M. Marinho and R. J. Chandler, *Geotechnique*, 1994, **44**, 551-556.

39.   Y. Guan and D. G. Fredlund, *Can Geotech J*, 1997, **34**, 604-614.

40.   A. J. Peck and R. M. Rabbidge, *Soil Sci Soc Am Pro*, 1969, **33**, 196-202.

41.   A. J. Peck and R. M. Rabbidge, *Science*, 1966, **151**, 1385-1386.

42.   G. H. de Rooij, M. J. v. d. Ploeg, H. P. A. Gooren, G. Bakker, C. W. Hoogendam, C. Huiskes, H. Kruidhof, L. K. Koopal, M. J. v. der Ploeg, G. H. de Rooij and M. J. van der Ploeg, *Biologia*, 2009, **64**, 438-442.

43.   M. J. van der Ploeg, H. P. A. Gooren, G. Bakker, C. W. Hoogendam, C. Huiskes, L. K. Koopal, H. Kruidhof and G. H. de Rooij, *Hydrology and Earth System Sciences*, 2010, **14**, 1787-1799.

44.   G. Bakker, M. J. van der Ploeg, G. H. de Rooij, C. W. Hoogendam, H. P. A. Gooren, C. Huiskes, L. K. Koopal and H. Kruidhof, *Vadose Zone J*, 2007, **6**, 196-202.

45.   W. P. Eaton and J. H. Smith, *Smart Materials & Structures*, 1997, **6**, 530-539.

46.   J. N. Israelachvili, *Intermolecular and surface forces*, Academic Press, Burlington, MA, 2011.

47.   P. S. Nobel, *Physicochemical and environmental plant physiology*, Academic Press, Inc., San Diego, 1991.

48.   S. Beeby, *MEMS mechanical sensors*, Artech House, Boston, 2004.

49.   K. Davitt, E. Rolley, F. Caupin, A. Arvengas and S. Balibar, *Journal of Chemical Physics*, 2010, **133**.

50.   W. Wagner and A. Pruss, *J Phys Chem Ref Data*, 2002, **31**, 387-535.

51.   IAPWS, Fredericia, Denmark, 1996.

52.   P.-G. de Gennes, F. Brochard-Wyart and D. Quéré, *Capillarity and wetting phenomena: drops, bubbles, pearls, waves*, Springer, New York, 2004.

53.   P. G. Debenedetti, *Metastable liquids: concepts and principles*, Princeton University Press, Princeton, N.J., 1996.

54.   T. D. Wheeler and A. D. Stroock, *Langmuir*, 2009, **25**, 7609-7622.

55.   T. D. Wheeler and A. D. Stroock, *Nature*, 2008, **455**, 208-212.

56.   V. Kaajakari, *Practical MEMS*, Small Gear Publishing, Las Vegas, NV, 2009.

57.   X. G. Zhang, in *Modern Aspects of Electrochemistry*, eds. C. G. Vayenas, R. White and M. Gamboa-Adelco, Springer US, 2005, vol. 39, ch. 2, pp. 65-133.

58.   R. Battino, T. R. Rettich and T. Tominaga, *J Phys Chem Ref Data*, 1984, **13**, 563-600.

59.   A. Salette, R. Lefevre, C. Déhan, P. Morfouli and L. Montès, *Procedia Engineering*, 2012, **47**, 426-429.

60.   P. J. French and A. G. R. Evans, *Solid-State Electronics*, 1989, **32**, 1-10.

61.   B. Bae, B. R. Flachsbart, K. Park and M. A. Shannon, *J Micromech Microeng*, 2004, **14**, 1597-1607.

62.   W. Kester, in *Sensor technology handbook*, ed. J. S. Wilson, Elsevier, Amsterdam; Boston, 2005, pp. 31-136.

63.   Y. Kanda, *IEEE Transactions on Electron Devices*, 1982, **29**, 64-70.

64.   F. Caupin, A. Arvengas, K. Davitt, M. E. Azouzi, K. I. Shmulovich, C. Ramboz, D. A. Sessoms and A. D. Stroock, *J. Phys.-Condes. Matter*, 2012, **24**.

65.   O. Vincent, D. A. Sessoms, E. J. Huber, J. Guioth and A. D. Stroock, *arXiv preprint arXiv:1402.6776*, 2014.

66.   F. Caupin and A. D. Stroock, in *Liquid Polymorphism*, John Wiley & Sons, Inc., 2013, pp. 51-80.

67.   C. Hall and W. D. Hoff, *Water transport in brick, stone, and concrete*, Spon Press, Abingdon, Oxon, OX; New York, NY, 2002.

Figure 1
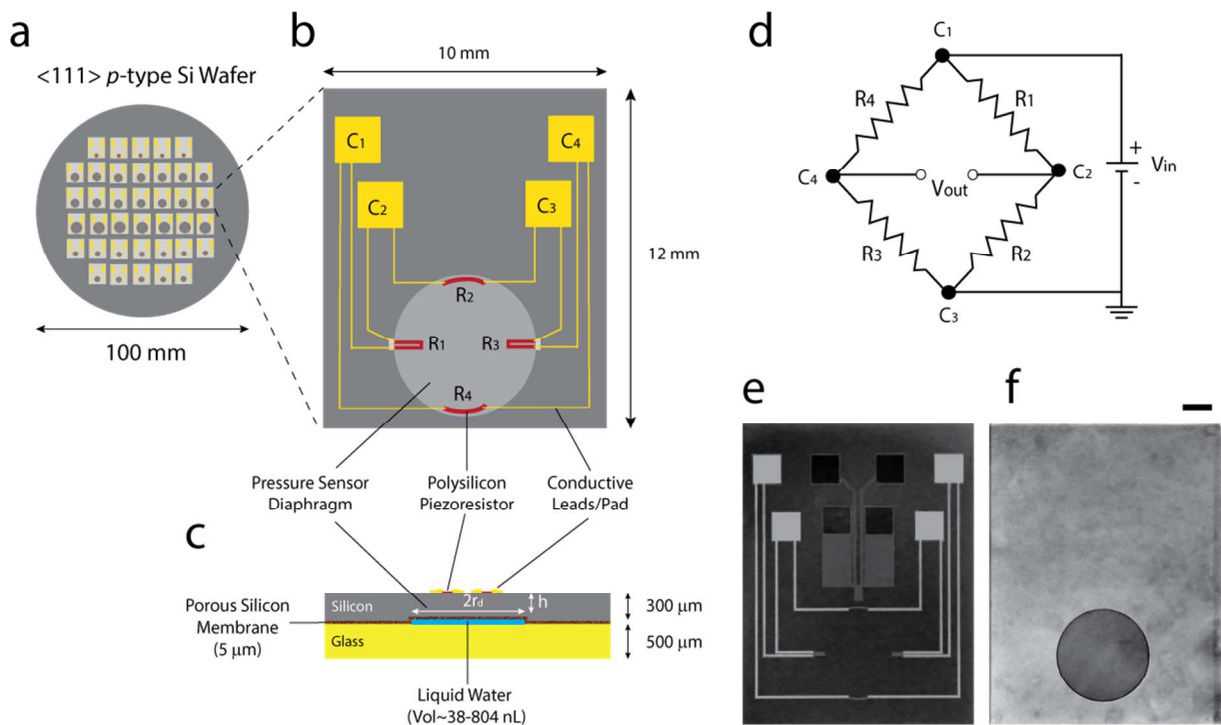
Fig. 1 Microtensiometer. **(a)** Organization of tensiometers on a 4" *p*-type <111> silicon wafer. Wafer contains 38 sensors with diaphragms of various radii: 0.7 mm (5 copies), 1 mm (12 copies), 2 mm (14 copies), and 3.4 mm (7 copies). **(b-c)** Top (b) and cross-sectional (c) views of a sensor with a 2 mm-radius diaphragm. Aluminum leads and contact pads are shown in yellow and polysilicon resistors are shown in red. In (b), contact pads for Wheatstone bridge are labeled C_1-C_4 and resistors are labeled R_1-R_4. In (c), the diaphragm radius and thickness are labeled r_d and *h*, respectively. **(d)** Wheatstone bridge configuration of piezoresistors and connections for applied (V_{in}) and measured (V_{out}) voltages. Labels of contact pads and resistors correspond to those in (b). **(e)** Photo showing top-view of an individual fabricated sensor (die) with 2 mm-radius diaphragm. Patterned oxide for a platinum resistance thermometer (PRT) is visible in the center, top of the die. No PRT was fabricated on the microtensiometers described in this paper. **(f)** Bottom-view of device shown in (e) showing the porous silicon membrane surface and circular cavity of depth ~ 25 µm. Scale bar = 1.5 mm.

Figure 2
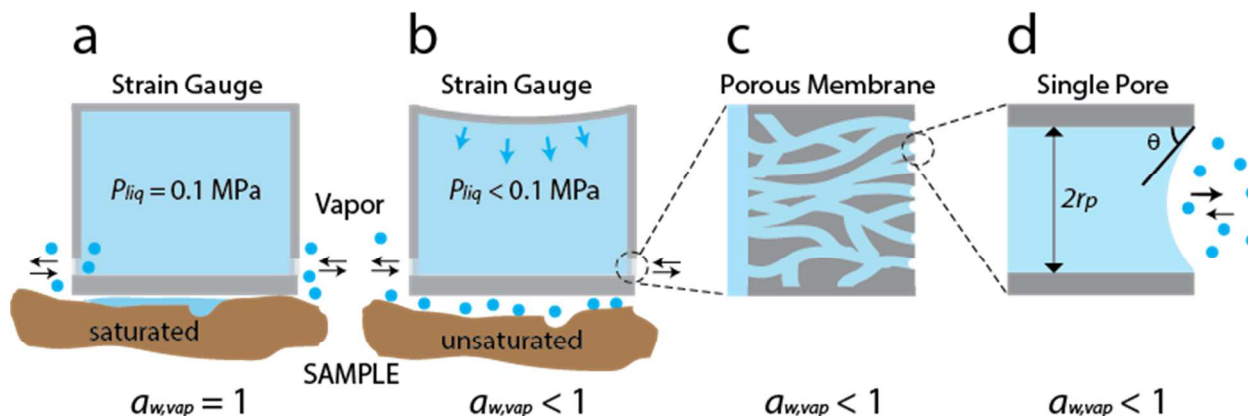
Fig. 2 Concept of tensiometry. **(a)** Bulk liquid in equilibrium ($P_{liq} = p_{vap} \cong 0.1$ MPa) with a saturated vapor ($a_w = 1$; tensiometer placed in a sample, e.g. saturated soil) through a porous membrane (shown in light grey on two lower sides of the cavity); liquid-vapor equilibrium exists and no evaporation occurs from the bulk liquid. **(b)** Sub-saturated vapors ($a_{w,vap} < 1$; tensiometer placed in unsaturated soil as an example) lower the hydrostatic pressure in the bulk liquid ($P_{liq} < 0.1$ MPa) until the capillary pressure of the air-liquid meniscus in the membrane is exceeded, resulting in evaporation of the bulk liquid. Changes in hydrostatic pressure are measured by measuring the deflection of a flexible diaphragm (strain gauge shown as curved plate on top side of cavity). **(c)** Porous membrane at the interface of the cavity couples external vapor with bulk water inside the cavity. **(d)** Close-up of a single pore within the membrane showing a concave air-liquid interface; r_p is the pore radius and θ is the contact angle of the liquid with the wall of the membrane.

Figure 3

(i)	Grow Thermal SiO2 LPCVD *p*+ Polysilicon	(v)	Anodic Bonding
(ii)	Pattern and Etch PolySi Resistors, SiO2	(vi)	Deposit, pattern, etch Aluminum pads, wires
(iii)	Pattern and Etch Backside Cavity	(vii)	Passivation Open Vias
(iv)	Electrochemically-Etch and Anneal Porous Si		

Legend: Al, PolySi, SiO2, Si, PoSi, Glass, SiO2+Si3N4
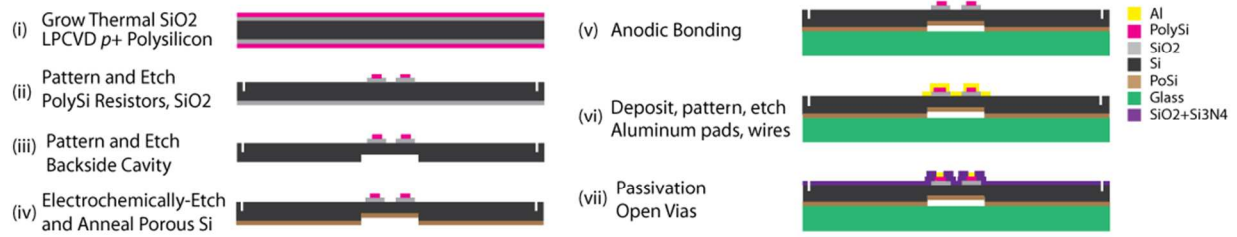
Fig. 3 Microtensiometer fabrication process flow (abridged). Detailed process flow provided in the supplemental section, Fig. S1.

Figure 4
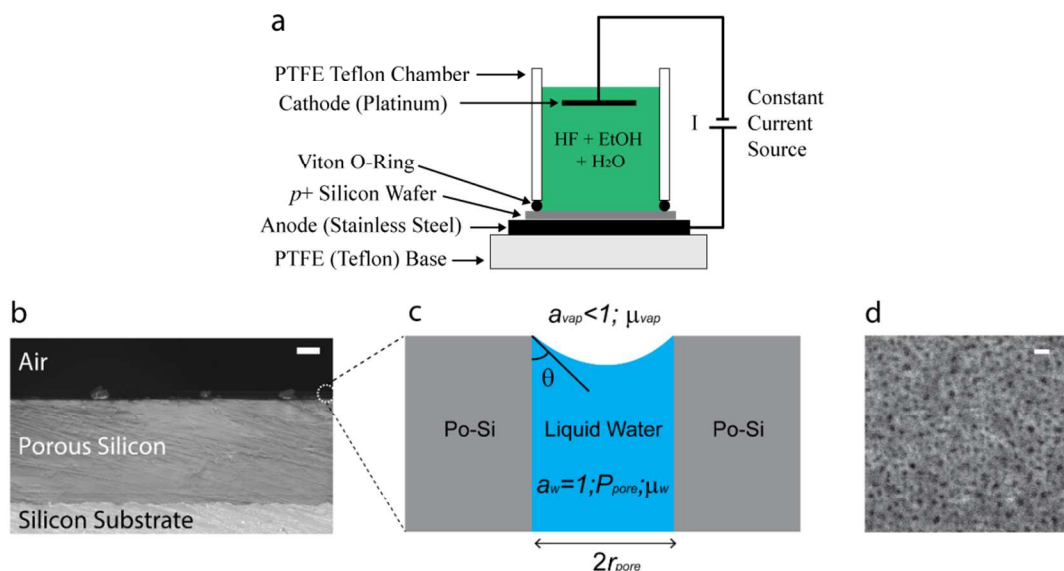
Fig. 4   Nanoporous silicon membrane. **(a)** Electrochemical etch cell (cross-section) used for the formation of porous silicon. **(b)** Scanning electron micrograph cross-section of porous silicon membrane; scale bar = 1 μm. **(c)** Schematic of an individual pore cross-section within the porous silicon membrane showing the liquid-vapor interface, the contact angle of water with the membrane wall (θ), and pore radius (r_{pore}). **(d)** Nanoporous silicon (grey), top view, showing surface pores (dark spots) with diameters ($2r_{pore}$) ranging from 1-5 nm; scale bar = 10 nm.

Figure 5
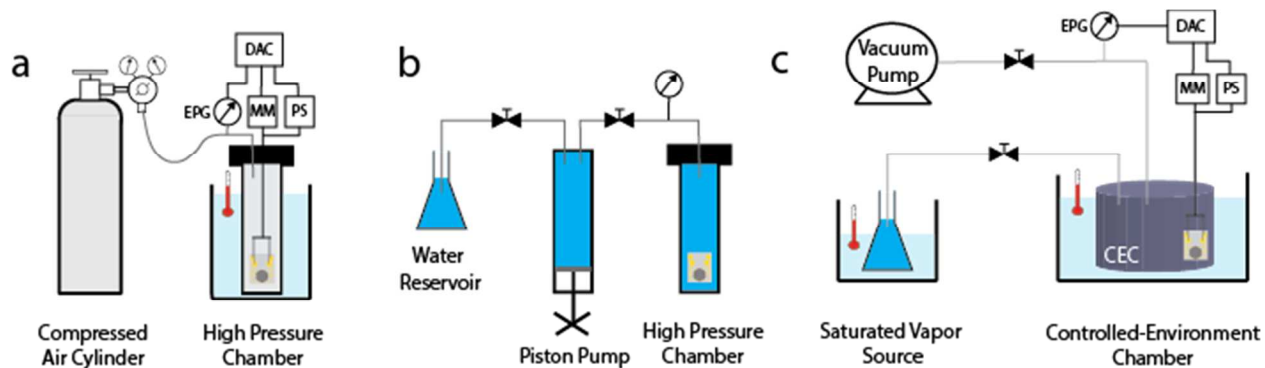
Fig. 5 Experimental setup for calibration, filling, and testing of the microtensiometer. **(a)** Positive pressure of air used to calibrate pressure sensor to $P_{air} > 10$ MPa at constant temperature. DAC=Data acquisition card + computer; MM=digital multimeter; PS=digital power supply; EPG=electronic pressure gauge. **(b)** Filling under high pressure ($P_{liq} > 5$ MPa) of water. **(c)** Controlled environment chamber (CEC; dark grey air-tight cylinder) used to equilibrate sensor with sub-saturated vapor stream for testing.

Figure 6

(a)

(b)
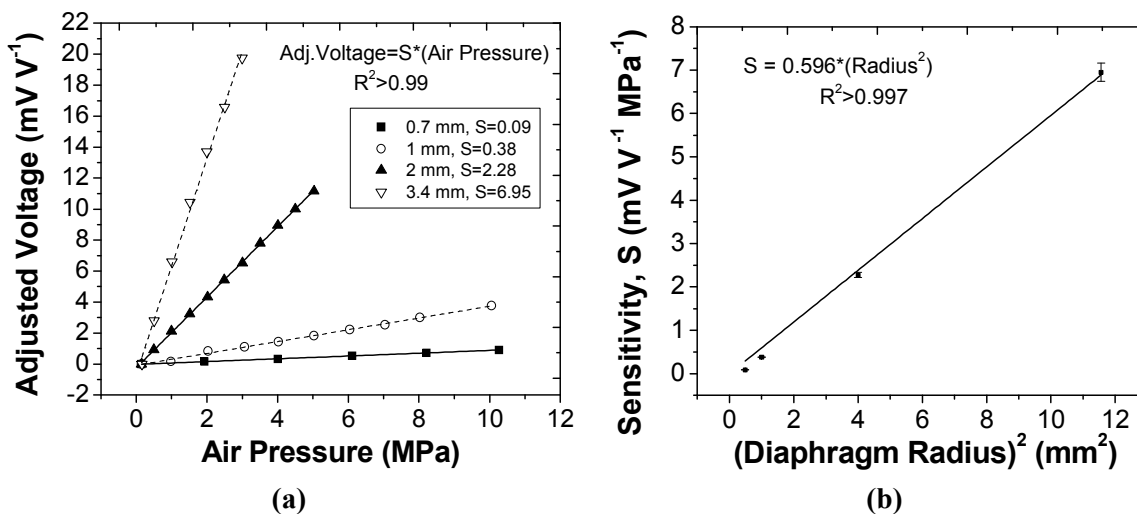
Fig. 6 Pressure sensor calibration: **(a)** Microtensiometer calibrations using positive pressures of air for diaphragms of different radii. The responses plotted were shifted by their offsets $((\Delta V_{out}/\Delta V_{in}) - (\Delta V_{out}/\Delta V_{in})_{os}$; eqn (7)). Legend: for each diaphragm radius in mm, the slope of the linear regressions represent the sensitivity, S [mV V^{-1} MPa^{-1}] (eqns (7), (8)). Offset voltages were: 28.5 mV V^{-1} (0.7 mm), 27.3 mV V^{-1} (1 mm), 3.8 mV V^{-1} (2 mm), and 27.5 mV V^{-1} (3.4 mm). Higher values of 'S' indicate greater sensitivity to pressure. **(b)** Sensitivity versus (diaphragm radius)$^2 = r_d^2$ (see eqns (7),(8)) for calibrations in (a).

Figure 7
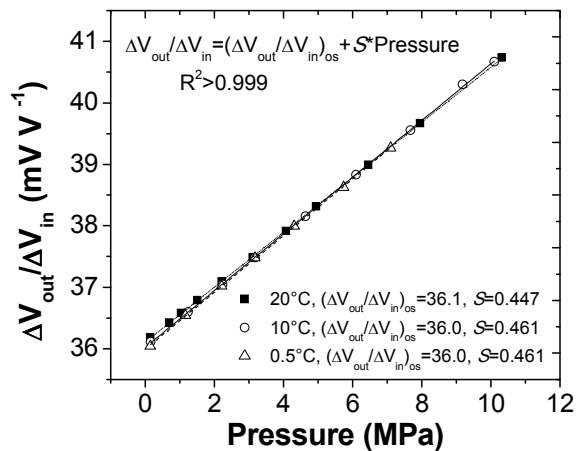
Fig. 7 Reproducibility and temperature-dependence of pressure sensor calibrations of a 1-mm radius diaphragm device at 20°C, 10°C, and 0.5°C. $(\Delta V_{out}/\Delta V_{in})_{os}$ [mV V^{-1}] is the voltage offset at $\Delta P=0$ MPa pressure, and S [mV V^{-1} MPa^{-1}] is the sensitivity.

33

Figure 8

(a)   (b)   (c)
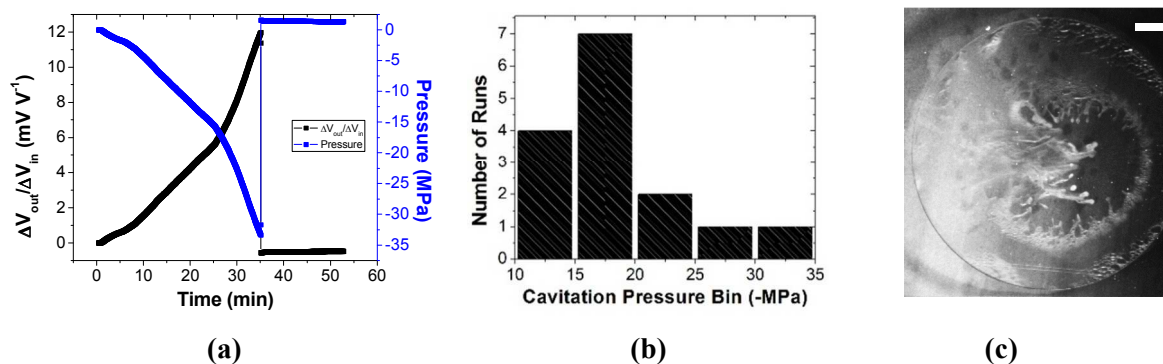
Fig. 8   Stability limit. **(a)** Transient response of a microtensiometer (1-mm radius diaphragm) exposed to ambient relative humidity ($a_w \sim 0.6 \equiv \Psi_w \cong$ -54 MPa). Voltage response ($\Delta V_{out}/\Delta V_{in}$ – black points and left axis) and pressure difference across diaphragm based on calibration (blue points and right axis) are shown. At 35 minutes, the liquid within the cavity cavitated and the pressure returned to a positive value. **(b)** Histogram of the stability limits of microtensiometers for 15 runs with 10 different sensors. **(c)** Snapshot of cavitation in the liquid cavity of a microtensiometer (3.4-mm radius diaphragm). Cavitation image captured using a high-speed camera (MotionPro HS-3, Redlake Imaging, Cheshire, CT) at 3000 fps through the glass wafer. See supplemental movie. Scale bar = 1 mm.

Figure 9
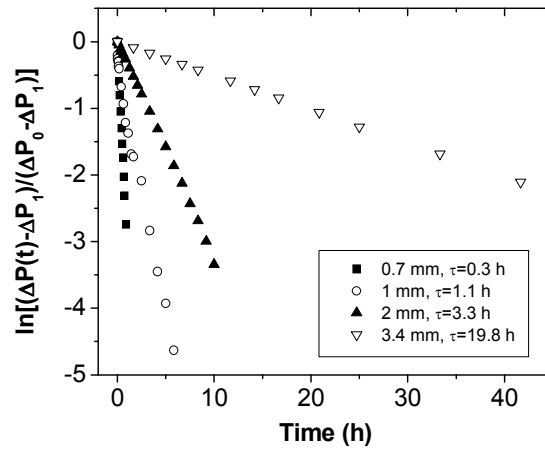
Fig. 9   Natural log plot of unaccomplished change in the difference in pressure across the diaphragm for different radii. The pressure differences are: instantaneous, $\Delta P(t)$; initial, ΔP_0; and final ΔP_1. Slopes of the linear regressions were used to estimate time constants of equilibration, τ, indicated in the legend (slope = $-\tau^{-1}$).

Figure 10
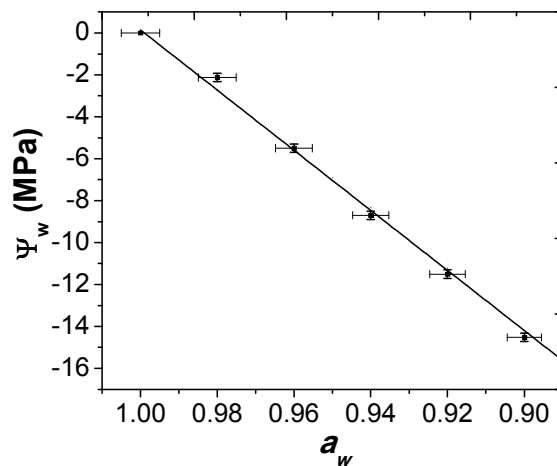
Fig. 10   Comparison to Equation of State. Measured (filled squares) and IAPWS-95 calculated (line) water potentials (Ψ_w, MPa) at various vapor activities (a_w) as defined by the vapor pressures in vacuum (Fig. 5c). Measurements were performed with a 1-mm radius diaphragm at 20°C. Error bars on water potential are the uncertainties reported in Table 2 and those on activity are dominated by the propagation of the uncertainty in temperature through eqn (4).

Table 1

Table 1	Comparison of conventional methods of hygrometry				
Method	**Range** Ψ_w **(MPa),** a_w	**Accuracy** $(\pm \Psi_w$ **MPa;** $\pm a_w)$	**Response Time**	**Measurement Area/Volume**	**Limitations**
Psychrometry[33, 34]	Ψ_w:-0.1 to -10 a_w:0.999 to 0.93	Ψ_w: ±0.1 a_w: ±0.001	1 min	< 5 cm²	Temperature-sensitive, installation expertise required
Electro-Magnetic[17, 25-27]	Ψ_w: -2.7 to -0.5 a_w: 0.98 to 0.996	Ψ_w: ±3 a_w: ±0.02	10-60 min	> 30 cm²	Low accuracy
Tensiometry[36]	Ψ_w:+0.2 to -0.16 a_w:1 to 0.999	Ψ_w:±5×10⁻⁴	30 min	> 10 cm²	Small range, requires maintenance

37

Table 2

Table 2 Mechanical and electronic characteristics of pressure sensors. Full scale is defined as the pressure difference across the diaphragm at 0.1% strain, a conservative estimate of the strain at fracture; linearity of the response of the Wheatstone bridge is not guaranteed across this full range. Uncertainty is represented in terms of both pressure (MPa) and percent of full scale.

Diaphragm Radius	Full Scale (FS) (pressure difference at 0.1% strain)	Sensitivity, S	Uncertainty	
(mm)	(MPa)	(mV V^{-1} MPa^{-1})	(MPa)	(% FS)
0.7	76.1	0.09	0.78	1.02
1	26.1	0.38	0.15	0.59
2	3.3	2.28	0.03	0.93
3.4	0.7	6.95	0.01	1.44

38